

A CONTINUOUS INDENTATION TEST FOR METALS

D. JARAMILLO V., S. KURIYAMA† and M. A. MEYERS

Department of Metallurgical and Materials Engineering, New Mexico Institute of Mining and Technology, Socorro, NM 87801, U.S.A.

(Received 19 May 1984; in revised form 5 June 1985)

Abstract—A penetration test using a continuously increasing load applied on a knife-edge indenter (30° angle) is described. The specific advantage of this method is that the applied load is continuously recorded as a function of the penetration depth. Ni-200 and 70/30 brass with varying plastic deformation responses produced by different cold rolling and annealing schedules were studied. The finite element method was applied to model the plastic deformation process under the indenter and to predict the load versus depth-of-penetration curves. A linear relationship between the applied load and the penetration depth was found experimentally and by computer simulation for all conditions.

Résumé—Nous décrivons un essai de pénétration qui utilise une charge augmentant continûment, appliquée sur un indenteur en lame de couteau (angle de 30°). L'avantage spécifique de cette méthode est que la charge appliquée est enregistrée continûment en fonction de la profondeur de pénétration. Nous avons étudié le Ni-200 et le laiton 70/30 en changeant les réponses à la déformation plastique produites par divers programmes de laminage et de recuits. Nous avons utilisé la méthode des éléments finis pour modéliser la déformation plastique sous l'indenteur et pour prévoir les courbes de la charge en fonction de la profondeur de pénétration. Dans toutes les conditions, nous avons trouvé expérimentalement et par simulation sur ordinateur, une relation linéaire entre la contrainte appliquée et la profondeur de pénétration.

Zusammenfassung—Es wird ein Eindringtest beschrieben, bei dem eine kontinuierlich ansteigende Last auf einen Stempel mit einer Messerkante (30° -Winkel) einwirkt. Der besondere Vorteil dieser Methode liegt darin, daß die angelegte Last kontinuierlich in Abhängigkeit von der Eindringtiefe verfolgt wird. Untersucht wurden Ni-200 und Messing 70/30, deren plastisches Verhalten sehr unterschiedlich war wegen der verschiedenen zur Herstellung benutzten Walz- und Ausheilverfahren. Der plastische Verformungsprozeß unterhalb des Eindruckstempels wurde mit der Methode der finiten Elemente berechnet; hiermit wurde der Zusammenhang zwischen Last und Eindringtiefe ermittelt. Für alle Bedingungen ergab sich ein linearer Zusammenhang zwischen angelegter Last und Eindringtiefe, sowohl experimentell als auch mit der Computersimulation.

1. INTRODUCTION

The hardness test is the most common mechanical test for metals. It produces an arbitrary number that is related to the strength of the material. On the other hand, the tensile test produces parameters that are of fundamental significance and that can be directly used in the design of structures. The ease of conducting the hardness test has led to numerous attempts to correlate the hardness to tensile parameters [1–5]. However, the plastic deformation under an indenter is complex; this is compounded by the dependence of flow stress on prior plastic deformation exhibited by metals (work hardening). Hence, simplified correlations of the form $H = k\sigma_y$, where H is the hardness (defined as load divided by projected area of indentation), k is a proportionality constant, and σ_y is the yield stress, have only been successful for specific metals over a limited range of plastic deformation response. The early theoretical attempts to derive correlations have used the slip-line-field (rigid

perfect plastic system) approach (Hill [6], Hill *et al.* [7]). Marsh [18] utilized the relationship $H = k\sigma_y$ and confirmed its validity for quartz and materials with a high ratio, σ_y/E , where E is Young's modulus. However, for lower values of σ_y/E , the mode of deformation involves a radial displacement of material, leading to a different equation. Hirst and Howse [9] used wedge indenters with angles between 60° and 170° and indented a variety of materials. They found that friction contributed to the process. For small wedge angles, and high σ_y/E ratios, they found that the deformation process was consistent with Hill's [6, 7] calculations. When these conditions were not met, substantial differences were observed. Johnson [10] explained the differences between the predictions of Hill's elasto-perfectly-plastic theory with observed results at low σ_y/E ratios and large angles in terms of a radial expansion of the material, which is not incorporated in Hill's theory. Johnson [10] then applied Hill's theory for the radial expansion of a spherical cavity to an indentation and arrived at relationship which provided a much more satisfactory correlation with experimental results. He

†Permanent address: The Institute of Physical and Chemical Research, Saitama, Japan.

proposed that the indentation pressure (force/area of indentation) was governed by the parameter $(E/\sigma_y) \tan [(\pi - \theta)/2]$ where θ is the wedge angle. The following equation describes this behavior

$$\bar{p} = \frac{\sigma_y}{\sqrt{3}} \left[1 + \ln \frac{4E}{3\pi\sigma_y} \tan \left(\frac{\pi - \theta}{2} \right) \right]. \quad (1)$$

Johnson [11] also developed the theory for an analogous problem: the deformation of a plastic wedge by a rigid plate.

Another approach, implemented by Shaw *et al.* [12, 13], used an elasto-plastic model. The work hardening of the metal is not incorporated into this treatment.

The work described herein is an attempt at obtaining fundamental strength properties (yield stress, work hardening coefficient, uniform elongation) by means of an indentation test and numerical analysis.

2. EXPERIMENTAL

2.1. Materials

Two different alloys were used in the present investigation: Nickel 200 (99.5% Ni) and 70% Cu–30% Zn brass. This material was cut into plates of dimensions $100 \times 65 \times 25.4$ mm, fully annealed, and then reduced by cold rolling (reductions of 20, 40, 60, 80 and 90% in area). Tension and indentation specimens from the materials with 80% of reduction by cold rolling were annealed at temperatures between 200 and 700°C for 1 h. Longitudinal and transverse tensile specimens were machined according to the ASTM E 8-68 designation, and chemically polished to remove any surface irregularities. Tensile testing was carried out using an MTS-810 universal testing machine. A strain rate of 0.001 s^{-1} was applied under stroke control. In order to record the elongation, an MTS clip-gage (12.7 mm gage length) extensometer was used.

Figure 1(a) shows a general conceptual sketch of the continuous indentation test. A sharp indenter ($\theta = 30^\circ$) is pressed into the specimen by the application of a load increasing at a constant rate. This load was plotted against the depth of the indentation directly on the X–Y recorder. In order to have plane-strain behavior, a knife-edge geometry was used. This indenter is sensitive to the anisotropy of the plastic deformation response which is an important characteristic of metals after processing. Specimens with parallel and polished surfaces were prepared for these experiments, along both the longitudinal and transverse directions (with respect to rolling). The characteristics of such indenter, as well as the loading set-up in the MTS universal testing machine, are shown in Fig. 1(b).

The MTS universal testing machine was used in the compression mode, and the load P vs depth of indentation t was continuously recorded by using the same extensometer described previously for the tension test. These experiments were conducted at a

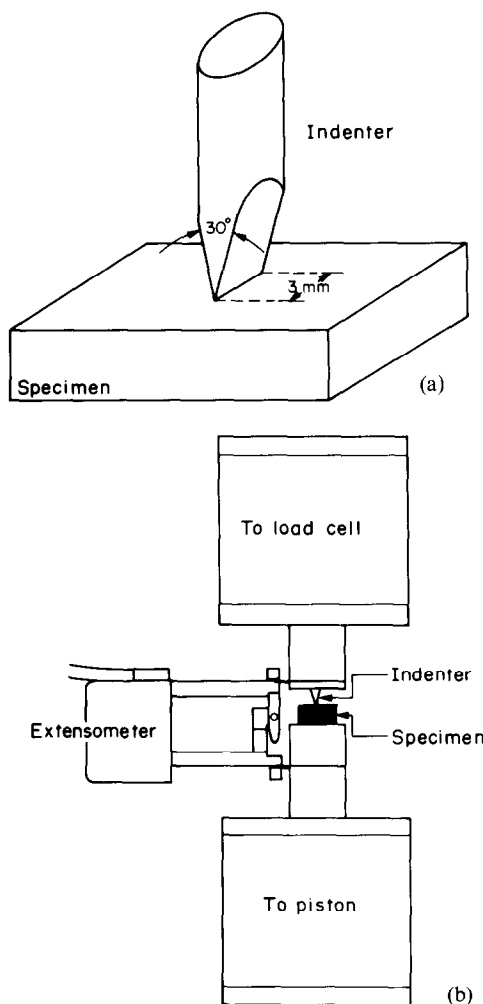


Fig. 1. (a) Knife-edge indenter and specimen; (b) complete indentation system.

piston velocity of 0.0125 mm s^{-1} under stroke control.

The material from which the indenters were machined is an AISI W1 steel, quench hardened from 700°C in water and tempered at 200°C. The jigs and holder for the experimental set-up were made of AISI 4140 steel quench hardened from 830°C in oil. In order to reduce friction, molybdenum sulfide powder or vacuum grease was applied to the specimen prior to penetration.

2.2. Finite element code

The finite element method for elasto-plastic materials was used to model the material flow under an indenter and to predict the theoretical load versus penetration depth curve for different material conditions.

Since material close to the central part of the knife-edge indenter does not flow in a direction parallel to the edge of the indenter during penetration, a condition of plane strain was assumed with boundary conditions given by the amount of displacement along the cross-sectional contour of the

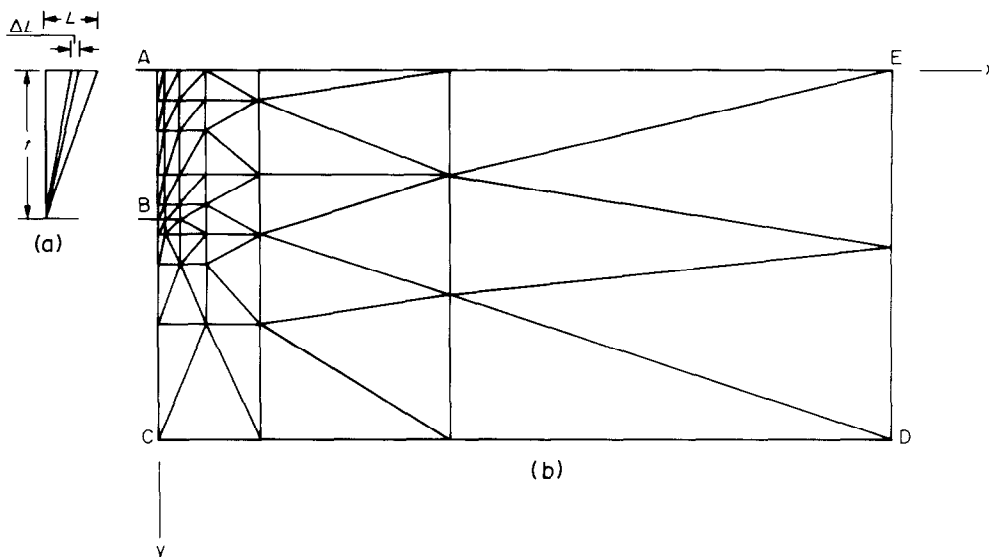


Fig. 2. (a) Displacements given to segment AB; (b) mesh division for finite element analysis.

indentation. For calculations, the indenter was assumed to be rigid, and the specimen was assumed to be an isotropic elasto-plastic material.

The finite element code applied to this study was developed based on a series of routines given by Swedlow [14] and using the documentation given by Nyo and Sinclair [15]. The principal features of this code are: (a) it is used for the plane strain deformation of elasto-plastic materials with work hardening obeying von Mises flow criterion, (b) the form of the elements is triangular, (c) the displacement function within the elements is expressed by a linear polynomial, and (d) the Gauss elimination method is used for obtaining the incremental displacements of the nodal points from a structural stiffness matrix. The relationship between the effective true stress $\bar{\sigma}$ and the effective natural logarithmic plastic strain $\bar{\epsilon}_p$ is introduced as the exponential equation $\bar{\sigma} = c(\bar{\epsilon}_p + \delta)^n$, where δ is defined as $(\bar{\sigma}_y/c)^{1/n}$, where $\bar{\sigma}_y$ is the effective yield stress. The rate of work-hardening H used in the formation of the stiffness matrix is calculated at every step of the iteration from the expression $H = (\bar{\sigma} - \bar{\sigma}^*)/(\bar{\epsilon}_p - \bar{\epsilon}_p^*)$ where $\bar{\sigma} > \bar{\sigma}^*$ and $\bar{\epsilon}_p > \bar{\epsilon}_p^*$. $\bar{\sigma}^*$ and $\bar{\epsilon}_p^*$ are values calculated at each step, and $\bar{\sigma}$ and $\bar{\epsilon}_p$ are values defined by the constitutive equation $\bar{\sigma} = c(\bar{\epsilon}_p + \delta)^n$. This definition of the work-hardening rate H suppresses the divergence of calculation automatically. Additionally, in order to minimize the divergence of calculation, the rate of work-hardening is taken to be zero [16] when the calculated stress $\bar{\sigma}^* > 1.05 \bar{\sigma}_y$, and is taken to be $5H$ when $\bar{\sigma}^* < 0.9 \bar{\sigma}_y$, where $\bar{\sigma}_y$ is defined as the theoretical value of stress obtained from the constitutive equation at the calculated plastic strain $\bar{\epsilon}_p^*$.

Figure 2(b) shows the mesh division used in this study for the analysis by the finite element method, where displacements shown in Fig. 2(a) are given on a boundary AB in the x direction. The number of

elements and nodal points in this mesh are 70 and 46, respectively. Calculations are repeated until an accumulation of incremental ΔL becomes a given displacement L .

For the mesh used in this study [Fig. 2(b)], the boundary points along BC move only in the y direction owing to symmetry of deformation; boundary points along CD and DE are fixed points; and the boundary EA is a free surface. The distance AB corresponds to the penetration depth where the presence of a crack is assumed; different displacement conditions are established according to the shape of the given crack. This deformation sequence is different from the one undergone by the actual penetration process. The depth of the crack is assumed constant in this analysis, with the penetration angle increasing as a function of the displacement. The Prandtl-Reuss plasticity theory and the von Mises flow criterion, deduced from an assumption of path independence, are used in this model; hence, both deformation processes lead to the same final deformation state through different deformation paths.

3. RESULTS AND DISCUSSION

3.1. Tensile tests

Figure 3 shows the engineering stress-strain curves for Ni-200. From these curves it is possible to observe an increase in the values of the yield and maximum stress with an increase in the percentage of cold rolling reduction. It can also be seen that the uniform elongation zone for these curves becomes very short with increasing reduction which indicates a small work hardening response of the materials previously cold rolled. On the other hand, curves for the materials with 80% cold rolling and annealing show a more extended uniform elongation zone, from

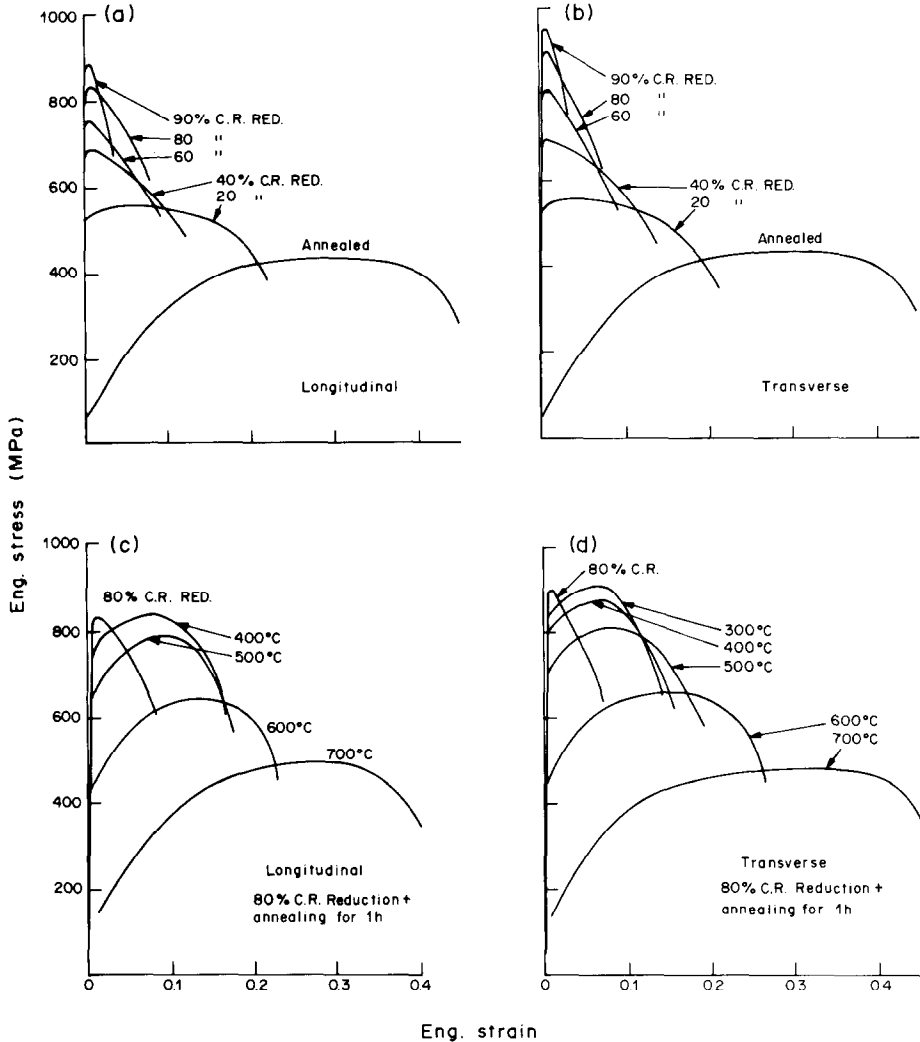


Fig. 3. Engineering stress-strain curves for Ni-200; (a) longitudinal and (b) transverse cold-rolled conditions; (c) longitudinal and (d) transverse after 80% cold reduction and different anneals.

which it is possible to determine the work hardening exponent accurately.

Small differences for the yield and maximum stress values are observed between longitudinal and transverse specimens (to the rolling direction) of Ni-200, but larger differences are observed for the 70/30 brass specimens.

To examine the tensile properties of Ni-200 and 70/30 brass after various degrees of cold rolling reduction, master curves of effective true stress, $\bar{\sigma}$, vs effective natural strain, $\bar{\epsilon}$, were obtained [Fig. 4(a) and (b)], by using the definitional equations of the effective stress and plastic strain [17]. These incorporate the plastic strain values induced during the cold rolling process (20, 40, 60, 80 and 90% reduction). The uniaxial true stress-strain curves for the as-rolled materials are shown in these figures with thinner lines, starting at a value of effective strain corresponding to the strain given in the rolling process. The upper curves in these figures represent the ultimate tensile stress found in the uniaxial true

stress-strain curves for rolled materials, while the lower curves represent the values of yield stress for the same materials. In these plots, the work hardening rate in the tensile tests is much higher than in cold rolling. If the two processes were identical, the yield stress and maximum stress curves would coincide with each other.

Due to the small uniform elongations exhibited by the engineering stress-strain curves for the cold rolled materials shown in Fig. 3, it was difficult to determine accurately the strain hardening exponent n . However, these values were found to be of the order of 0.05–0.1 for the deformed materials (Ni-200 and 70/30 brass); for the rolled and annealed conditions they were found to be between 0.44 and 0.5 for Ni-200 and between 0.1 and 0.23 for 70/30 brass. No substantial differences between the values obtained for longitudinal and transverse specimens were observed. A plot of uniform elongation versus the strain hardening exponent is shown in Fig. 5. From this figure it seems that Considère's criterion [18], which predicts

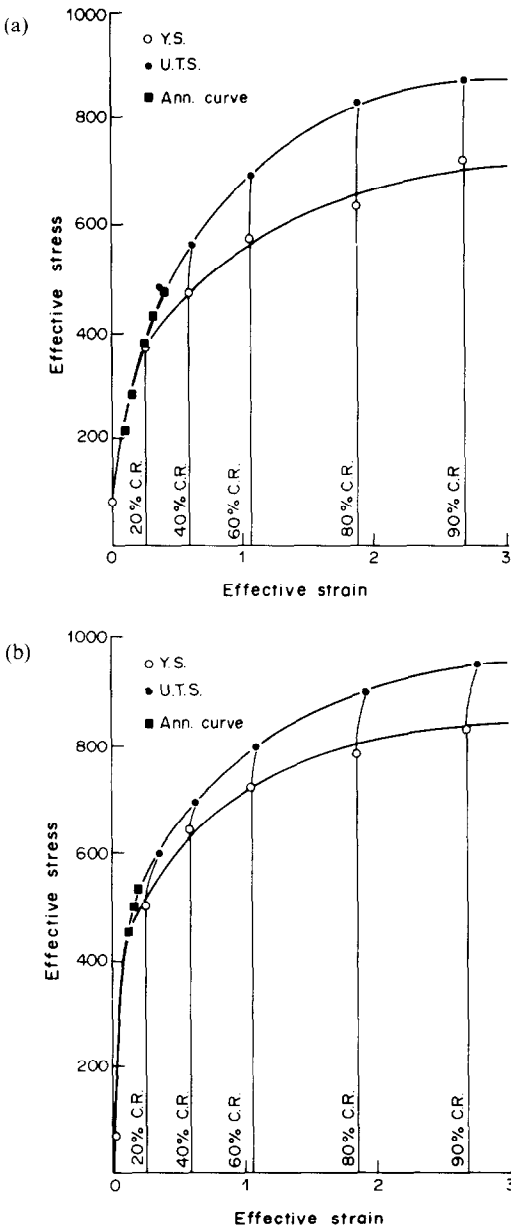


Fig. 4. Master curve of effective true stress-effective natural strain, incorporating tensile and rolling properties of (a) Ni-200 and (b) 70/30 brass after various degrees of cold rolling reductions.

a straight line with slope equal to 1, applies approximately to Ni-200, but does not apply at all to 70/30 brass. Indeed, for brass the uniform elongation is approximately equal to twice the value of the work hardening exponent.

3.2. Penetration tests

Figure 6 shows the results of the penetration tests for Ni-200 longitudinal specimens in the cold-rolled and cold rolled (80%) plus annealed conditions. The cold-rolling reductions and annealing temperatures are marked in Fig. 6(a) and (b), respectively. The most important characteristic of these tests is that the

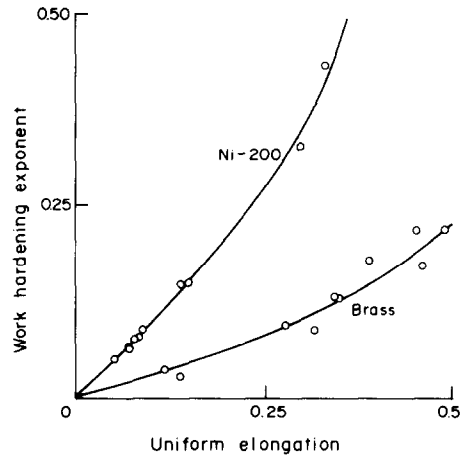


Fig. 5. Uniform elongation vs work hardening exponent for Ni-200 and 70/30 brass.

curves can be considered as straight lines, to a first approximation. The results for the transverse specimens are essentially identical to the ones for the longitudinal specimens. The results for 70/30 brass (not shown) can also be approximated as straight

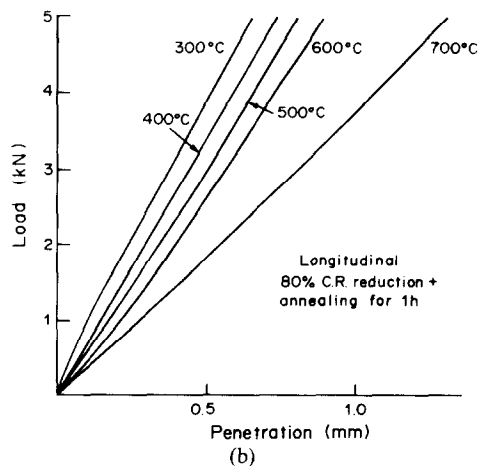
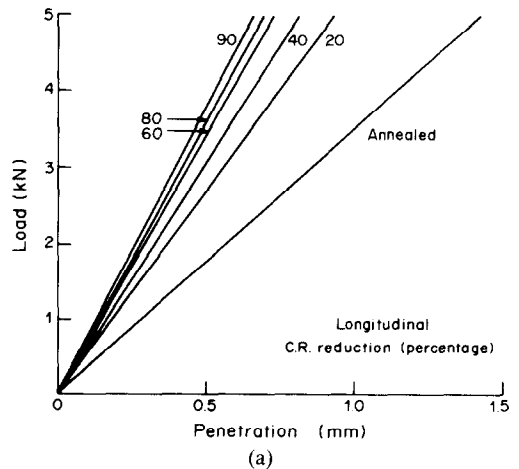


Fig. 6. Load vs penetration curve for Ni-200; (a) annealed and cold-rolled (reductions of 20, 40, 60, 80, 90%) conditions; (b) cold-rolled (reduction of 80%) and annealed for 1 h at 300, 400, 500, 600, 700°C.

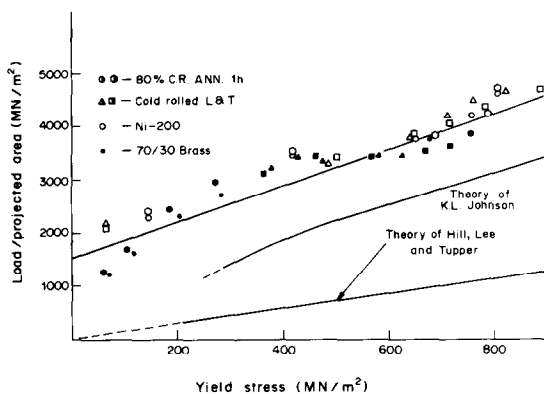


Fig. 7. Load-projected area ratio vs yield stress experimentally determined for Ni-200 and 70/30 brass and theoretical predictions [7]. Black symbols: Ni-200; hollow symbols: 70/30 brass; \triangle cold rolled, longitudinal; \square cold rolled, transverse; \circ cold rolled and annealed for 1 h.

lines. The differences in slope among the various conditions are found to be consistent with the differences in tensile response, as will be discussed later.

In order to determine the reproducibility of the test, eight experiments were conducted on the same annealed 70/30 brass specimen. The slopes of the load, P , vs penetration depth, t , curves were determined and converted into load/projected area ratios P/A . This is done by multiplying the former by 0.622, because P/A is represented by $P/(2lt \tan 15^\circ)$ where l is the width of the indenter. A mean value of the ratio P/A is found to be 1.8 MN/m^2 with a standard deviation of 0.07 MN/m^2 . This yields a standard error of $\sim 4\%$. This test is therefore very reproducible.

The load/projected area ratios for all conditions (both Ni-200 and 70/30 brass) are plotted as a function of yield stress (obtained in the uniaxial tensile test) in Fig. 7. The experimental data can be represented by a straight line as

$$\frac{P}{A} = (3.6 \pm 0.2) \sigma_y + (1.459 \pm 130) \text{ (in MN/m}^2\text{)}. \quad (2)$$

The terms inside the brackets and preceding the \pm signs are the standard deviations. The square of the correlation factor, R^2 , is 0.857. When penetration occurs into a material which shows no elastic limit but has a parabolic work-hardening, a force is necessary for penetrating due to work hardening. The work-hardening increases the flow stress of the regions plastically deformed. Hence, the line which fits the experimental points does not pass through the origin. The results displayed in Fig. 7 are in contrast with simple hardness tensile data correlations which predict a proportionality between the load/projected area and the yield stress

$$H = \frac{P}{A} = C \sigma_y. \quad (3)$$

Prandtl [15] was the first to explain the origin of the constraint factor, C . He considered a flat rigid punch

and calculated the load required to produce plastic deformation in the specimen. He found that $C = 3\pi/2 = 2.57$. Hill [6] used the slip-line-field analysis and found the same result. Shield [20] extended the treatment of Hill [6] and found $C = 2.82$. A more elaborate theory was developed by Hill *et al.* [7]; for wedges they calculated the load required for penetration as a function of indenter angle for a plane-strain configuration and a knife-edge indenter. For $\theta = 30^\circ$, one finds a value of $C = 1.4$, using Fig. 8 of Hill *et al.* [7]. Hill *et al.*'s [7] prediction is plotted in Fig. 7; one can clearly see that it is not realistic. Johnson [11] developed equation (1) for wedges having large values of θ . He assumed a radial expansion of the material. Applying equation (1) one obtains the curve shown in Fig. 7; the correlation with the observed data is much better than Hill *et al.*'s theory. The limitation of the aforementioned and other treatments [19, 20] is that work hardening is not incorporated into the computations, leading to a proportionality between H and σ_y . On the other hand, the deformation process under a real indenter and for a material that work hardens is much more complex than in a non-work-hardening case; the flow stress increases with plastic deformation. The net result is that the resistance to penetration is increased due to work-hardening. The simple analytical models and the slip-line-field theory do not consider this effect. The finite element code described in Section 3.3 incorporates this effect successfully.

An attempt to obtain the ductility from the continuous indentation test parameters was made based on Böklen's [21] concepts, taking into account the differences shown by the deformation around the indentation, where piling-up occurs for the rolled materials and sinking-in is observed for the perfectly annealed ones (Fig. 8). A plot of h/r ratio (where h is the height of the pile-up region and r is its length; it is the extension of the plastic deformation on the surface of the specimen) vs uniform elongation u is shown in Fig. 9. The experimental data are represented by an exponential curve as

$$\ln\left(\frac{h}{r}\right) = -(0.195 \pm 0.067) - (8.81 \pm 0.35) u. \quad (4)$$

The numbers in the brackets preceding the \pm signs are the standard deviations. The square of the correlation factor R^2 is 0.972.

The presence of pile-up in a material is explained by the fact that plastic deformation takes place at constant volume, and the volume displaced by the indenter produces an extrusion near the edges of the penetration. Meyers *et al.* [22] have found that the shape of this pile-up region is directly related to the plastic response of the material. Qualitatively, the shape difference is easily explained by looking at the extension of the plastic deformation throughout the specimen. If the material work hardens, the flow stress of the regions plastically deformed increases, forcing further plastic deformation in regions

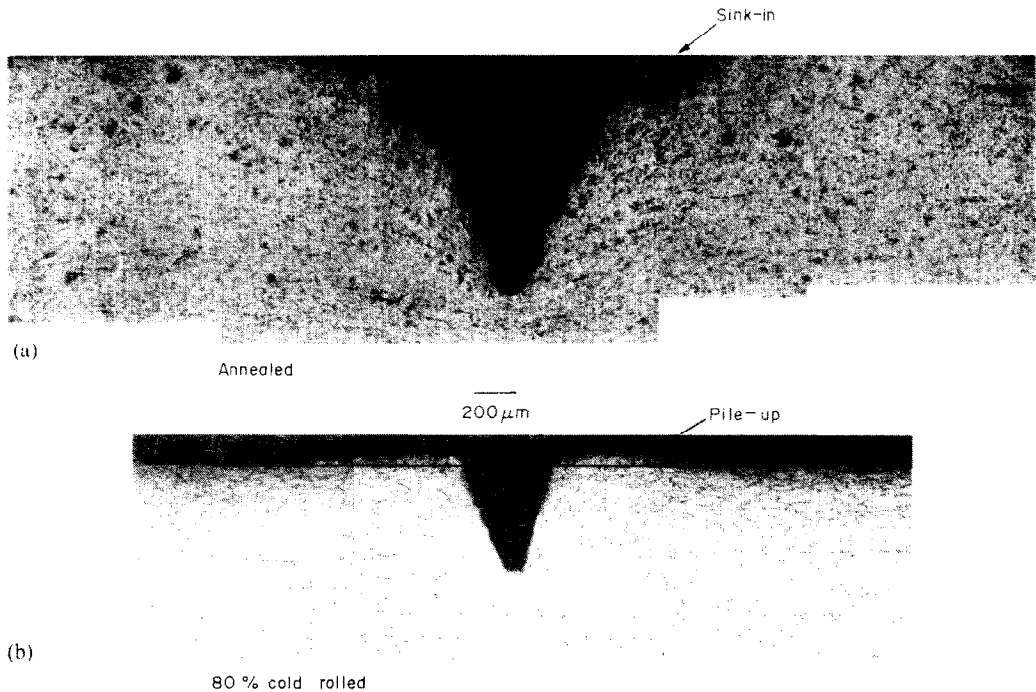


Fig. 8. Sinking-in and piling-up (a) in annealed and (b) 80% cold rolled Ni-200.

further and further away from the indentation. An extended plastic deformation region is produced, by virtue of the constancy of volume, and a diffuse pile-up results.

3.3. Deformation process during indentation

Simulations of the deformation process taking place during indentation were conducted by using the FEM code, in which penetration depths were 0.25, 0.5 and 1.0 mm and materials were Ni-200 and brass 70/30 in the annealed condition and with different degrees of cold-rolling reduction.

The relationship between the effective true stress $\bar{\sigma}$

and the effective natural plastic strain, $\bar{\epsilon}_p$, used in the code as the constitutive equation, is

$$\bar{\sigma} = c(\bar{\epsilon}_p + \delta)^n \tag{5}$$

Material constants of equation (5) for Ni-200 are, for example, $\bar{\sigma}_y = 69.0$ MPa, $c = 780.0$ MPa, $\delta = 0.741 \times 10^{-4}$, and $n = 0.255$ for the annealed condition; and $\bar{\sigma}_y = 789.0$ MPa, $c = 953.0$ MPa, $\delta = 0.524 \times 10^{-3}$, and $n = 0.025$ after 80% rolling reduction.

The deformation process of Ni-200 in the annealed and 80% cold rolled conditions is illustrated for a penetration depth of 0.50 mm in Fig. 10. Figures 11 and 12 show the isostrain and isostress contours obtained from the numerical results for annealed and 80% cold rolled Ni-200, respectively. There are differences between the stress and strain fields of the annealed and the deformed material. The isostrain and isostress contours for the deformed material (80% cold rolled Ni-200) concentrate in a region closer to the indenter than for the annealed material; this difference results in the formation of a bigger pile-up in the case of the deformed material. No difference in the computational results for the deformation process was obtained for the different depths of penetration. This leads to a proportionality between the applied load and the indentation depth. This is due to a similarity which is based on using the same mesh division and the same boundary conditions for different indentation depths and applying different amounts of displacements along the indentation edge. These displacements are varied proportionately to the mesh dimensions. This prediction is in good agreement with the experimental load versus

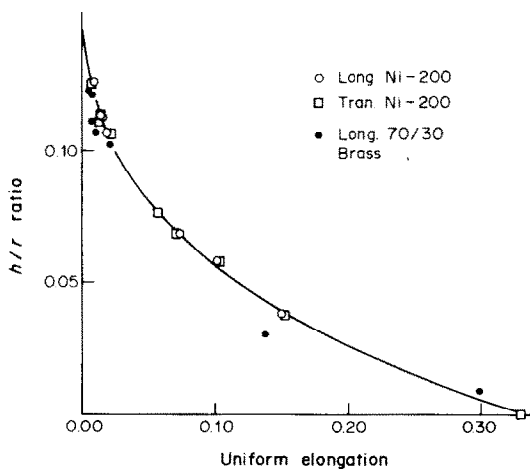


Fig. 9. Ratio h/r vs uniform elongation u in Ni-200 and 70/30 brass (where h and r are height and width of pile-up region, respectively).

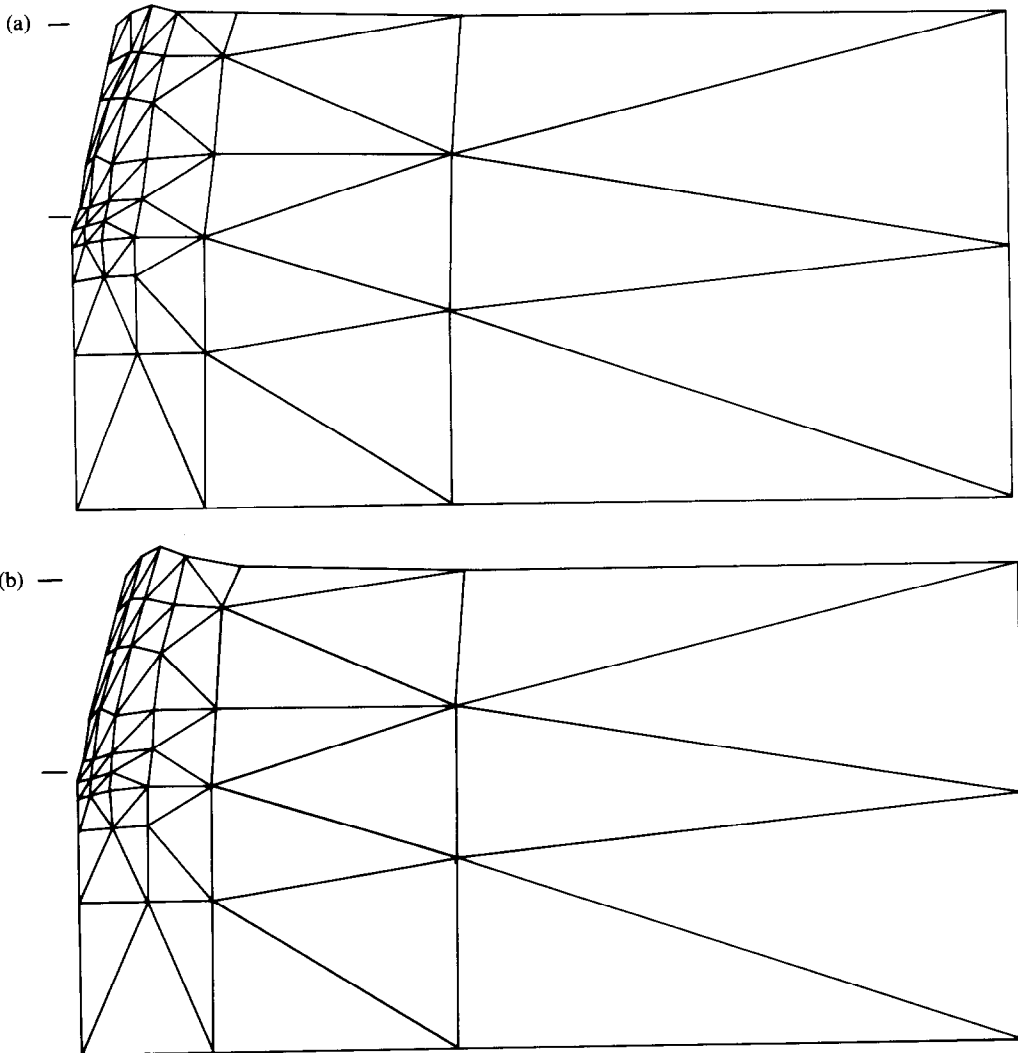


Fig. 10. Deformation of finite-element mesh after indentation for (a) annealed Ni-200 and (b) Ni-200 cold rolled to a reduction in thickness of 80%.

penetration depth plots (Fig. 6) which show a proportionality between load and penetration depth.

3.4. Penetration forces

Penetration forces were calculated from the values of applied forces at the nodal points along the indentation edge, by using the conservation of energy criterion. This consideration gives an equation of the form

$$P\Delta h = P(\Delta h_d + \Delta h_s) = \sum f_{xi}\Delta x_i + \sum f_{yi}\Delta y_i + \sum f_{fci}\Delta l_i + \Delta E_{ef} \quad (6)$$

where $f_{fci} = f_{ni}\mu$.

P is the penetration force, and Δh is an apparent penetration depth of the indenter, which consists of a true penetration depth Δh_p and a shortening of the indenter Δh_s . f_{xi} and f_{yi} are the nodal forces acting along the indentation edge with the incremental displacements Δx_i and Δy_i in the x and y direction, respectively. f_{fci} and f_{ni} are the frictional force and

normal force at the nodal points along the indentation edge, respectively, Δl_i is the distance along which the frictional force moved, and μ is the coefficient of friction. ΔE_{ef} is the incremental energy for the crack formation. Equation (6) states that the external work done by the indenter (product of load and displacement) is equal to the sum of the work done by the surface tractions (decomposed along the x and y axes), the work done to overcome friction, and the work needed to create the new surface (crack extension). The term $P\Delta h_s$ is the elastic strain energy of the indenter and is actually a correction term. The distribution of the nodal forces along the indentation edge obtained for penetration depths of 0.50 mm for the annealed and 80% cold rolled conditions of Ni-200 are shown in Fig. 13. Also observable in this figure is a clearance formed near the tip of the indenter due to the stress field created by the displacements acting in the x direction when the penetration is taking place. This means that these displacements

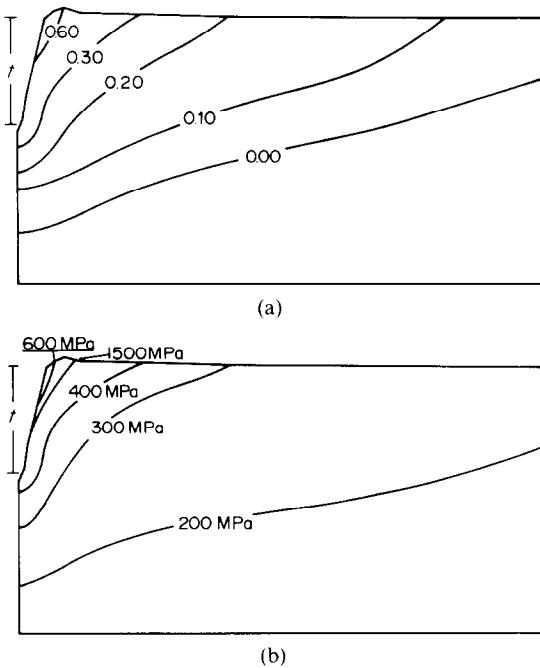


Fig. 11. (a) Isostrain contours of $\bar{\epsilon}_p$ and (b) isostress contours of $\bar{\sigma}$ for penetration depth of 0.5 mm in annealed Ni-200.

are larger than the ones required by the indenter. By using the indenter with a diameter of 3.0 mm and a length of 14.45 mm including the part of the 30° wedge (Young's modulus = 2.1×10^5 MPa) the displacement correction due to elastic deformation was made as shown in Fig. 14(a). The direct and corrected plots of penetration load vs indentation depth are

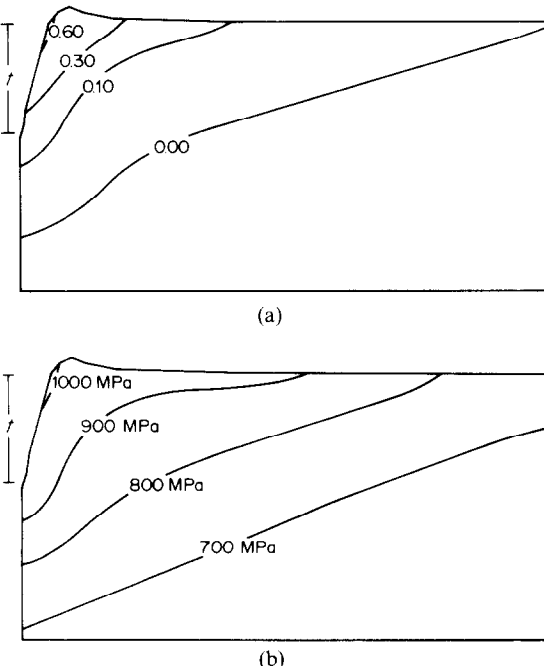


Fig. 12. (a) Isostrain contours of $\bar{\epsilon}_p$ and (b) isostress contours of $\bar{\sigma}$ for penetration depth of 0.5 mm in Ni-200 cold rolled to a reduction in thickness of 80%.

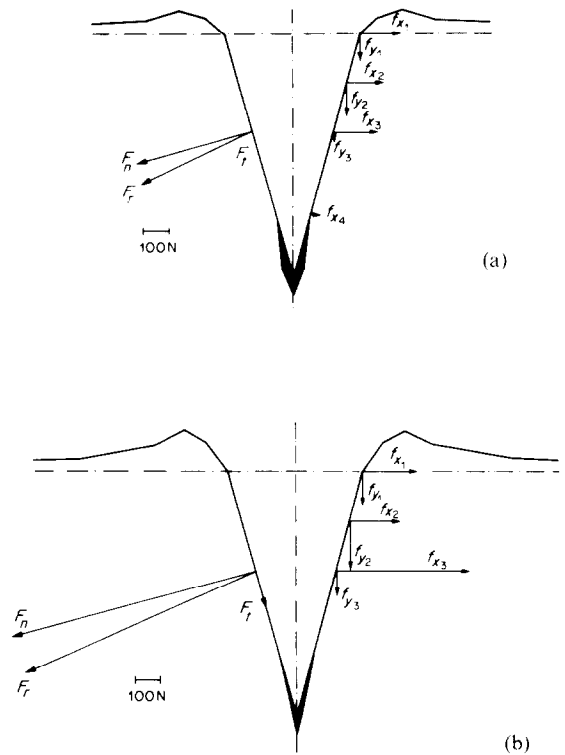


Fig. 13. Distribution of nodal forces along indentation edge for 0.50 mm penetration depth (a) in annealed and (b) 80% cold rolled Ni-200.

shown by a thick and a thin solid line, respectively. A schematic representation of the energy distribution during the penetration process is also shown in Fig. 14(a). The friction on the surface of the indenter is considered to be between sliding and stick-slipping because the indenter penetrates into a specimen making new surfaces on it due to crack formation. Therefore, indentation forces were calculated for the two cases of sliding and stick-slipping; the coefficient of friction was assumed to be 0.1 for sliding [23] and 0.3 for stick-slipping [24]. The results of these calculations are shown in Fig. 14(b), where experimental data which have already undergone displacement correction (elastic shortening of the indenter) are shown by solid lines; results for sliding ($\mu = 0.1$) are shown by dashed lines passing through analytically determined points, and the ones for stick-slipping ($\mu = 0.3$) are shown by dash-dotted lines.

When friction of the indenter is assumed to be based on sliding, the penetration forces calculated are far lower than the observed forces (dashed lines). Additional load and energy are needed in order to match the experimental data. To explain this difference, the friction is assumed to be based on stick-slipping, so that the calculated penetration force increases and becomes close to the actual force (dash-dotted lines).

Another factor which affects the calculated load is the energy needed for crack formation. The surface energy for nickel is $\gamma = 2280 \text{ erg cm}^{-2}$ [25]; the area

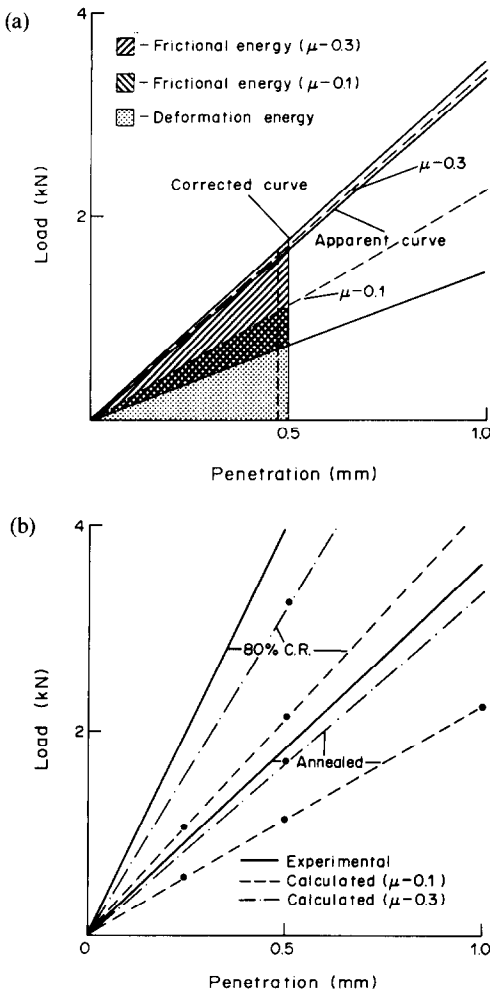


Fig. 14. (a) Schematic representation of correction for elastic shortening of indenter and of the energies during the penetration process. (b) Computer results for load-penetration depth curves after correction for elastic shortening of indenter.

under the indentation is 1.46 mm^2 . Hence, a value of about $33.28 \times 10^{-7} \text{ Nm}$ for crack formation is obtained. This value is very small in comparison with the energy required for penetration to the same depth (0.850 Nm) and can be therefore neglected.

Three different boundary conditions in the y direction along the indentation edge are assumed in order to simulate the deformation processes of piling-up and sinking-in: (1) the boundary condition (in the y direction) is set free; (2) the boundary conditions are

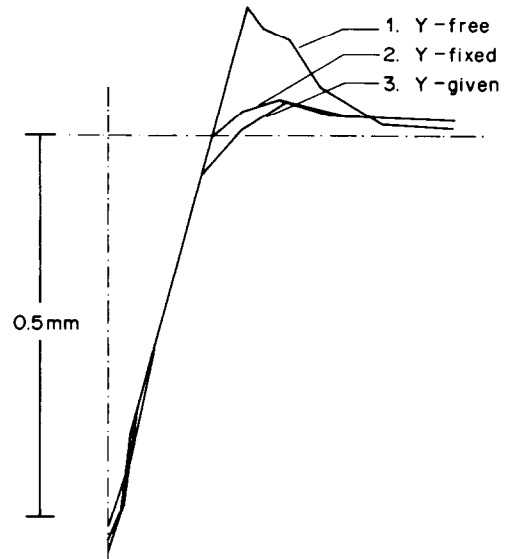


Fig. 15. Indentation profiles for annealed Ni-200 (0.50 mm penetration depth) under different boundary conditions for displacements in y direction.

fixed to establish the profile shown in Fig 8(b); and (3) the boundary conditions are defined by the displacements of the sinking-in profile shown in Fig. 8(a). The other boundary condition (the x direction) is established by the displacements for all cases, and the boundary conditions near the tip of the indenter are always free in both x and y directions, so that a small clearance is produced between the indenter and a specimen as shown in Fig. 13. A comparison of displacements and estimates of the forces according to the three different boundary conditions are shown in Fig. 15 and Table 1. It is observable from Table 1 that the indentation force P_i calculated for the given displacement condition is higher than for the cases of free and fixed conditions. Hence, one can conclude that the establishment of the boundary condition has an effect on the load vs penetration curve.

The load/projected area ratios were calculated for both 70/30 brass and Ni-200 after different amounts of work hardening, and for three different conditions: non-friction ($\mu = 0.0$), sliding friction ($\mu = 0.1$), and stick-slipping friction ($\mu = 0.3$). They are plotted against the yield stresses in Fig. 16 and numerical results for Ni-200 and brass 70/30 are shown, respectively, by continuous lines and dashed lines.

When the friction is assumed to be by stick-slipping the calculated results are very close to the experi-

Table 1. Force needed for deformation of specimen F_{def} , frictional force F_{fc} in case of $\mu = 0.1$, and indentation force P_i for different boundary conditions in y direction along the indentation edge

Boundary condition	Nodal forces ^a		Normal force F_n	Tangential force F_t	Force for deformation of specimen F_{def}	Frictional force F_{fc}	Indentation force P_{total}
	$\sum f_{xi}$	$\sum f_{yi}$					
$y = \text{free}$	362	0	350	98	765	231	996
$y = \text{fixed}$	458	212	498	87	717	301	1018
$y = \text{given}$	456	254	521	8	817	299	1116

^aAll forces are given in Newtons.

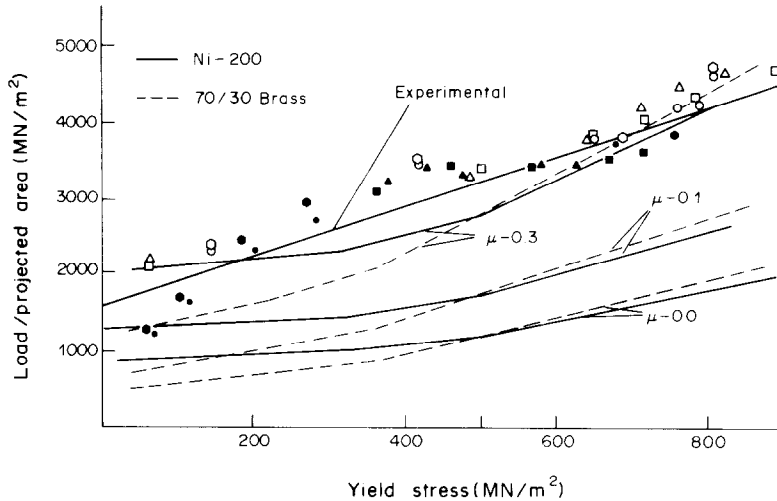


Fig. 16. Comparison of experimental relationship between load-projected area ratio and yield stress with numerical results obtained for three different conditions: of non-friction ($\mu = 0.0$), of sliding friction ($\mu = 0.1$) and stick-slipping friction ($\mu = 0.3$).

mental data, especially in the regions of low and high yield stresses. When the friction is not considered, the calculated results are given by two lines of $\mu = 0.0$ in the figure, and represent forces needed for the plastic deformation of specimen produced by an indenter. The force needed for penetration was also analyzed by Hill *et al.* [7] by applying the slip-line-field theory to the deformation of perfect plastic material as shown by a solid line in the figure. Our calculated forces for $\mu = 0.0$ are considerably larger than their results; this difference is due to work hardening incorporated into the computations. However, the numerical results are far lower than the experimental data if the friction force is not considered. As the yield stress increases due to the work-hardening (after pre-deformation), the stress-strain curve becomes close to a perfect plastic curve, to which the slip-line field theory can be applied with good approximation. From this fact, the calculated results obtained from the FEM are inferred to increase linearly according to the increase of yield stress beyond a certain yield stress; the slip-line-field theory also predicts a linear increase. However, the slopes of the former and the latter are different because of the frictional force.

3.5. Plasticine model

Modeling of the deformation process by an indenter was conducted using plasticine. One of the models consisted of fine alternated strips of black and white plasticine with free lateral boundaries as shown in Fig. 17(a). This model was penetrated by a relatively small indenter. The penetration profile from this model is sinking-in and resembles the deformation process taking place in annealed materials shown in Fig. 15. Here, the lines are deformed downwards in the vicinity of the indentation, while the region under the tip of the indenter showed no deformation. This fact is in accordance with the

deformation process obtained from computer simulations.

Another model using a fine printed grid under fixed lateral boundary condition was indented with a relatively large indenter. In this case the deformation process near the indenter is piling-up and resembles the numerical result of free condition in the *y* direction shown in Fig. 15.

From these results, it is concluded that the deformation processes of piling-up and sinking-in are affected by not only metal flow related to the work-hardening, but also by the boundary conditions of the specimen penetrated, namely, relative size between the indenter and the specimen thickness. Hence, the size of the specimen should be considerably larger than the indentation.

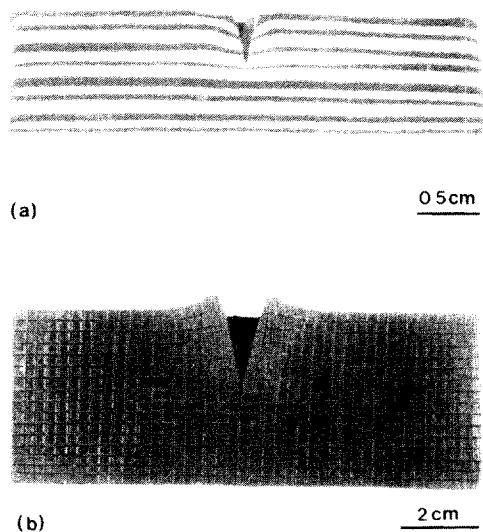


Fig. 17. Plasticine model showing (a) sink-in and (b) pile-up.

4. CONCLUSIONS

From the experimental and numerical results for Ni-200 and brass 70/30 using a continuous indentation test, the following conclusions are obtained:

1. A continuous indentation test for metals which is statistically reliable was developed.

2. A linear relationship between applied load and penetration depth of the materials is obtained for this continuous loading test with the slope of this line being a function of the metallurgical history.

3. The results obtained from the test developed can be related to tensile parameters by equations (2) and (4).

4. The finite element code developed for this study was used to simulate plastic deformations around an indentation edge taking place during penetration and the surface profiles in the cases of piling-up and sinking-in. The results of the computer simulation for the required load for penetration were found to be lower than the experimental values, due to the influence of the frictional forces during the penetration process. When the friction is assumed to be close to stick-slipping ($\mu = 0.3$), calculated results are in good agreement with the experimental results.

Acknowledgement—The authors gratefully acknowledge support of this research program by National Science Foundation Grant DMR 81-15127. CONACYT (Mexican Research and Technology Council) and ESQIE-IPN (Mexican Polytechnic Institute) provided support which allowed one of us (D.J.V.) to pursue this study. Deep appreciation is extended to Dr R. J. Salzbrenner (Sandia National Laboratory) for cold-rolling the specimens, to Dr P. Follansbee (Los Alamos National Laboratory) for advice on the utilization of the computer code, and to Dr J. L. Swedlow (Carnegie-Mellon University) for permission to use the code. Professor A. Singh graciously performed the computations of the standard deviations and R values for equations (2) and (4).

REFERENCES

1. D. Tabor, *Hardness of Metals*. Clarendon Press, Oxford (1951).
2. J. H. Westbrook and H. Conrad (editors), *The Science of Hardness Testing and its Research Applications*. Am. Soc. Metals, Ohio (1971).
3. J. Motteff, T. K. Bhargava and W. L. McCoullough, *Metall. Trans. A* **6A**, 1101 (1975).
4. K. Furuya and J. Motteff, *Metall. Trans. A* **12**, 1303 (1981).
5. M. Demirkol and S. E. Kisakurek, *Mater. Sci. Engng.* **59**, 197 (1983).
6. R. Hill, *The Mathematical Theory of Plasticity*. Clarendon Press, Oxford (1950).
7. R. Hill, E. H. Lee and S. J. Tupper, *Proc. R. Soc.* **188A**, 273 (1947).
8. D. M. Marsh, *Proc. R. Soc.* **279A**, 420 (1947).
9. W. Hirst and M. G. J. W. Howse, *Proc. R. Soc.* **A311**, 429 (1969).
10. K. L. Johnson, *J. Mech. Phys. Solids* **18**, 115 (1970).
11. K. L. Johnson, *J. Mech. Phys. Solids* **16**, 395 (1968).
12. M. C. Shaw and G. J. de Salvo, *Trans. Am. Soc. Min. Engrs* **92**, 469 (1970).
13. M. C. Shaw and G. J. de Salvo, *Metall. Engng. Q.* **12**, 1 (1972).
14. J. L. Swedlow, *Computers Struct.* **3**, 879 (1973).
15. C. Nyo and G. B. Sinclair, Documentation of PLANDJ: A constant strain triangle finite element code for elastic problems, Carnegie-Mellon University, Pittsburgh, Pa (1978).
16. S. Kuriyama, H. Hayashi and S. Yoshida, *Proc. 4th Int. Conf. on Production Engineering*, Tokyo, p. 38 (1980).
17. G. E. Dieter, *Mechanical Metallurgy*, 2nd edn, p. 90. McGraw-Hill, New York (1976).
18. A. Considère, *Ann. Ponts Chaussées*, Vol. 9, ser. 6, p. 574 (1885).
19. L. Prandtl, *Nachr. Ges. Wiss. Gottingen, Math. Phys. Kl.*, p. 74 (1929).
20. R. T. Shield, *Proc. R. Soc.*, **233A**, 267 (1955).
21. R. Böklen, Ref. [2], p. 109.
22. M. A. Meyers, L. E. Murr, C. Y. Hsu and G. A. Stone, *Mater. Sci. Engng* **57**, p. 113 (1983).
23. B. Avitzur, *Metal Forming: Processes and Analysis*, p. 475. McGraw-Hill, New York (1968).
24. F. P. Bowden and D. Tabor, *The Friction and Lubrication of Solids*, p. 107. Clarendon Press, Oxford (1954).
25. L. E. Murr, *Interfacial Phenomena in Metals and Alloys*, p. 125. Addison-Wesley, Reading, Mass. (1975).